FULL PAPER

Enhanced Hydrogen Production by Photoreforming of Renewable Oxygenates Through Nanostructured Fe_2O_3 Polymorphs

Giorgio Carraro, Chiara Maccato, Alberto Gasparotto, Tiziano Montini, Stuart Turner, Oleg I. Lebedev, Valentina Gombac, Gianpiero Adami, Gustaaf Van Tendeloo, Davide Barreca, and Paolo Fornasiero**

Sunlight-driven hydrogen production via photoreforming of aqueous solutions containing renewable compounds is an attractive option for sustainable energy generation with reduced carbon footprint. Nevertheless, the absence of photocatalysts combining high efficiency and stability upon solar light activation has up to date strongly hindered the development of this technology. Herein, two scarcely investigated iron(III) oxide polymorphs, β- and ε-Fe_2O_3, possessing a remarkable activity in sunlight-activated H_2 generation from aqueous solutions of renewable oxygenates (i.e., ethanol, glycerol, glucose) are reported. For β-Fe_2O_3 and ε-Fe_2O_3, H_2 production rates up to 225 and 125 mmol h^{-1} m^{-2} are obtained, with significantly superior performances with respect to the commonly investigated α-Fe_2O_3.

1. Introduction

Almost 100 years after the Ciamician suggestion[1] to trust in solar energy technologies to overcome problems related to fossil fuels, the scientific community is still investing great efforts in the search for sustainable energy alternatives. In the last decade, remarkable worldwide attention has been devoted to the production of hydrogen which, besides being a key reactant for the chemical industry, is a strategically appealing energy vector.[2] In particular, solar hydrogen generation through photoelectrochemical and photocatalytic water splitting has received a considerable attention as a possible solution to the energetic and environmental problems raised by the use of conventional resources.[3–7] Nevertheless, in spite of several efforts, the conversion efficiency reached in water photosplitting is still too low to meet the standards required by large-scale applications.[4,8–10] An alternative approach for H_2 generation consists in the photoreforming of aqueous solutions containing oxygenated organic compounds (OOCs), such as ethanol, glycerol, and glucose, that can be expressed as:

$$C_nH_mO_k + (2n - k)H_2O \rightarrow nCO_2 + (2n + m/2 - k)H_2 \quad (1)$$

Such routes enable the conversion of sunlight, an intrinsically renewable resource, into molecular hydrogen, through the combination of photo-activated OOC oxidation and water splitting. If compared to the latter, OOC photoreforming is a less endoergonic process that also minimizes the back-reaction with oxygen, offering thus a more viable route for H_2 production.[9–11] Remarkably, the above OOCs can be sustainably produced from largely available biomasses, thus reducing the ecological footprint. Further environmental advantages arise from the possibility of using photoreforming also for polluted H_2O purification, through mineralization of waste products (such as alcohols, organic acids, etc.) arising from biomass processing industries. On the other hand, when OOCs are only partially oxidized, the process can profitably enable the obtainment of added-value by-products.[2,8,12]

According to reaction (1) and to the H_2 combustion heat versus the pertaining values for the target OOCs, the use of photo-reformed H_2 offers an important energy benefit with respect to the direct use of OOCs as fuels. Indeed, H_2 moles produced per each OOC mole according to Equation 1 are

Dr. G. Carraro, Dr. C. Maccato, Dr. A. Gasparotto
Department of Chemistry – University of Padova and INSTM
via F. Marzolo, 1 – 35131, Padova, Italy
Dr. T. Montini, Dr. V. Gombac, Prof. P. Fornasiero
Department of Chemical and Pharmaceutical Sciences – ICCOM-CNR Trieste Research Unit – University of Trieste and INSTM, via L. Giorgieri 1 – 34127, Trieste, Italy
E-mail: pfornasiero@units.it
Dr. S. Turner, Prof. G. Van Tendeloo
EMAT – University of Antwerp – Groenenborgerlaan 171 – 2020, Antwerpen, Belgium
Dr. O. I. Lebedev
Laboratoire CRISMAT, UMR 6508 CNRS-ENSICAEN, Bd. Maréchal Juin 6 – 14050, Caen CEDEX 4, France
Prof. G. Adami
Department of Chemical and Pharmaceutical Sciences – University of Trieste, via L. Giorgieri, 1 – 34127, Trieste, Italy
Dr. D. Barreca
CNR-IENI and INSTM – Department of Chemistry – University of Padova, via F. Marzolo, 1 – 35131, Padova, Italy
E-mail: davide.barreca@unipd.it

DOI: 10.1002/adfm.201302043

characterized by a higher energy content with respect to the OOC starting material.

The development of stable and efficient photocatalysts for H_2 production from OOCs should allow the worldwide diffusion of small plants for the operation of such processes, an advantage of key importance to overcome challenges related to H_2 distribution and storage. The use of H_2 in a fuel cell or in an internal combustion engine rather than of OOCs also results in a cleaner energy generation process, with no greenhouse gases emission, significantly reducing the environmental impact.[13] Hence, the conversion of renewable raw materials into H_2 using solar light represents a sustainable and more efficient way of producing energy with respect to the direct use of OOCs. Finally, if compared to photo-electrochemical routes, no further external energy inputs are required, an interesting feature for eventual large-scale applications.

In spite of the technological potential of photoreforming processes, their large-scale utilization is actually hindered by the availability of photocatalysts joining a high activity and service life under sunlight irradiation. Hence, the development of novel materials featuring ad-hoc properties is a key challenge still far from being completely satisfied. Besides being low-cost, abundant, and non-toxic, an ideal photocatalyst should properly harvest light with minimal electron/hole (e^-/h^+) recombination and efficiently drive the target chemical processes.[9] In this regard, among metal oxides, α-Fe_2O_3 (hematite) has emerged as a promising system for photocatalytic H_2 production, especially in the form of nanomaterials. Nevertheless, α-Fe_2O_3 performances are still limited by its low absorption coefficient, high recombination losses, and short diffusion length of photogenerated charge carriers.[14,15]

Motivated by the search for alternative iron oxide photocatalysts combining the inherent hematite advantages and enabling, at the same time, to overcome its shortfalls, in this article we report on a thorough investigation of supported Fe_2O_3 nanomaterials for photo-assisted H_2 production. As described in the following, the photocatalyst properties have been tuned by a careful control of phase composition and nano-organization. In particular, the optimization of a chemical vapor deposition (CVD) route involving an iron(II) molecular precursor[16] enabled the selective production not only of the well-known and most studied α-Fe_2O_3 phase, but also of the scarcely investigated β- and ε-Fe_2O_3 polymorphs[17] and, for the first time, their use in photoreforming processes. The synthesis and functional investigation of these two polymorphs represent an appealing strategy to overcome the hematite drawbacks. As a matter of fact, under simulated sunlight, the β- and ε-phases show enhanced photocorrosion resistance and yield H_2 evolution rates from ethanol aqueous solutions which are superior to α-Fe_2O_3 and considerably high in the framework of similar photocatalytic processes. In addition, β- and ε-Fe_2O_3 are very active even in the presence of more complex, though more sustainable, OOCs, namely glycerol and glucose, rendering the present approach extremely attractive and versatile in view of technological applications.[8]

2. Results and Discussion

The iron oxide phase composition was investigated by X-ray diffraction (XRD; Supporting Information, Figure S1). As can be observed, the choice of appropriate synthesis conditions enabled the selective preparation of α-, β-, or ε-Fe_2O_3, each of them free from other iron(III) oxide polymorphs. On α-Fe_2O_3, signals at 2ϑ = 24.2°, 33.1°, and 35.6°, ascribable to (012), (104), and (110) reflections of rhombohedral hematite were detected (PDF card 00–033–0664). For β-Fe_2O_3, the pattern was characterized by signals located at 2ϑ = 23.2°, 33.0°, and 38.4°, assigned to (211), (222), and (400) planes of cubic bixbyite (PDF card 00–039–0238). Finally, the orthorhombic ε-Fe_2O_3 presented the main signals located at 2ϑ = 29.9°, 32.9°, 35.2°, 36.4°, and 49.2°, related to the (013), (122), (200)/(130), (201), and (142)/(015) reflections, respectively (ICSD 51122). An overview of the crystal structures for the three different polymorphs, along with relevant structural details, is presented in Figure S1 (Supporting Information).

The photocatalyst morphological organization as a function of its phase composition was investigated by field emission-scanning electron microscopy (FE-SEM). For α-Fe_2O_3 (Supporting Information, Figure S2), the growth process resulted in a relatively compact deposit (average thickness = 800 nm), characterized by protruding sparse pyramidal-like structures (mean lateral size = 400–500 nm). β- and ε-Fe_2O_3 (Supporting Information, Figure S1) displayed a more uniform surface texture, with faceted nanopyramids (mean lateral size = 200 nm) yielding an average deposit thickness of 450 nm. The system composition was preliminarily investigated by energy dispersive X-ray spectroscopy (EDXS). Irrespective of the obtained polymorph, a C Kα signal close to noise level throughout the deposited thickness was recorded, highlighting the purity of the obtained materials (Supporting Information, Figure S3). The parallel trends for oxygen and iron confirmed the common chemical origin of these elements. Further valuable information was obtained by X-ray photoelectron spectroscopy (XPS) analyses, that, irrespective of the target polymorph, evidenced the formation of iron(III) oxide. This was testified by the Fe2p signal, whose $Fe2p_{3/2}$ and $Fe2p_{1/2}$ spin-orbit components were always located at Binding Energies (BEs) of 711.2 eV and 725.0 eV, respectively (Supporting Information, Figure S4a).[7,18]

The photocatalytic H_2 evolution under simulated solar irradiation for α-, β-, and ε-Fe_2O_3 was investigated in ethanol/water solutions (**Figure 1**). Control experiments demonstrated that the bare silicon substrate did not contribute to the observed hydrogen production. After an initial stabilization period, the three polymorphs promoted a remarkable hydrogen evolution, that remained stable at least up to 20 h of irradiation. The catalytic activity increased in the order α-Fe_2O_3 < ε-Fe_2O_3 < β-Fe_2O_3, yielding mean H_2 production rates of 40, 125, and 225 mmol h^{-1} m^{-2}, respectively. Basing on the above reported thickness values and assuming bulk densities for Fe_2O_3 polymorphs (see Experimental Section for details), hydrogen production rates of 10, 60, and 100 mmol h^{-1} g^{-1} were estimated, candidating the present nanomaterials among the most efficient photocatalysts ever reported for similar processes.[2,4,5,8,12,13,19,20] It is worth highlighting that the above yield values are slightly underestimated, since calculation of the catalyst mass has been performed by considering the target systems as compact deposits with bulk densities.

As a comparison, highly active black titania functionalized with Pt particles, one of the state-of-the-art photocatalytic

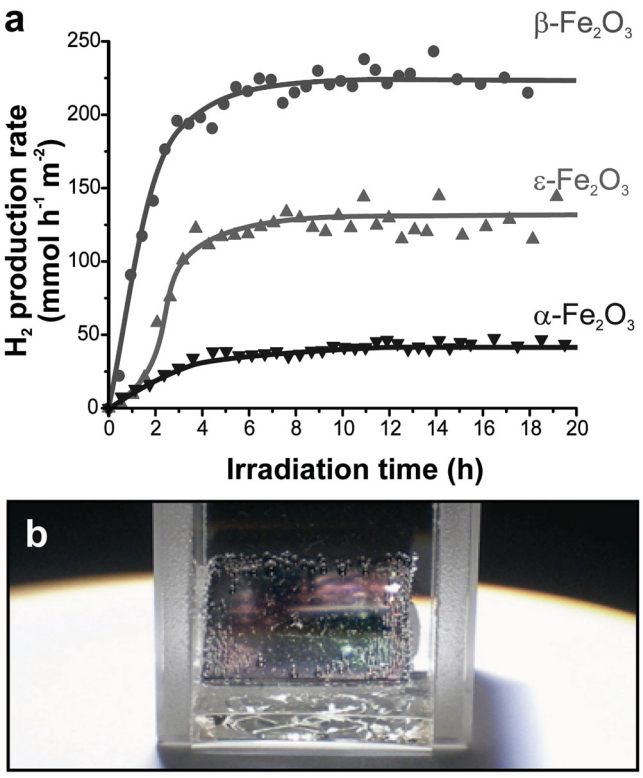

Figure 1. a) H_2 production rates from α-, β-, and ε-Fe_2O_3 by photoreforming of ethanol/water solutions upon simulated sunlight irradiation. Points are experimental data, while lines are for guidance only. b) Image of β-Fe_2O_3 immersed in an ethanol/water solution irradiated with simulated sunlight, evidencing the formation of H_2 bubbles.

materials, produces 10 mmol h^{-1} g^{-1} of H_2 using methanol, more reactive than the presently used ethanol.[21] In addition, ethanol photoreforming over Au-Pt/TiO_2 catalysts resulted in a maximum hydrogen evolution rate of 1.7 mmol h^{-1} g^{-1} under simulated solar irradiation.[22]

Beside presenting the lowest activity per gram of catalyst, as discussed above, α-Fe_2O_3 also underwent a partial leaching under operation. In fact, the analysis by graphite-furnace atomic absorption spectroscopy (GF-AAS) revealed the presence of 11.6 μg L^{-1} of Fe in the ethanol/water solution collected from the photocatalytic experiment, indicating that ≈ 4% of the catalyst was dissolved after 20 h of use. In a different way, the iron amounts present in the solutions recovered from the experiments with β- and ε-Fe_2O_3 were below the instrumental detection limit (± 0.8 μg L^{-1} of Fe). This finding indicates that leaching phenomena were negligible for β- and ε-Fe_2O_3, a very important result in view of technological applications. The understanding of Fe leaching mechanism is a complex issue, as the process is affected not only by pH changes during the photoreaction, but also by the surface status of each Fe_2O_3 polymorphs at a nanoscale level, with particular attention to the presence of defects. The interactions between the chelating carboxylic acids, generated by the partial oxidation of OOCs, with surface iron centers, have also to be taken into account. In this context, it has been demonstrated that a decrease of pH values for the reaction media can promote a partial iron(III) leaching, more significant in the case of amorphous iron(III) oxides with respect to nanocrystalline iron(III) oxide (α-Fe_2O_3) catalysts.[23] Therefore, these important aspects need to be further addressed in future studies.

Under simulated sunlight, solar-to-fuel efficiencies (SFE) for the three Fe_2O_3 polymorphs were estimated to be 0.16% for α-Fe_2O_3, 0.86% for β-Fe_2O_3, and 0.48% for ε-Fe_2O_3. Such data corroborate the great interest for the scarcely investigated β and ε-Fe_2O_3 polymorphs in view of hydrogen production by means of solar irradiation.

It is worth noting that, under the presently adopted conditions, ethanol was not fully converted into CO_2, but only partially oxidized, giving rise to the formation of acetaldehyde as the main product. In addition, 1,1-diethoxyethane, another important fine chemical, was also detected in the liquid phase (Supporting Information, Figure S5, Scheme S1, and Equation S1).

In the case of photo-reforming of OOC solutions catalyzed by semiconductor (SC) systems, like in the present case, the mechanism leading to hydrogen photo-production starts with the generation of e^-/h^+ pairs and involves the OOC dissociative chemisorption on the SC surface. In the case of ethanol, the simplest OOC used in this work, the mechanism and the fate of photogenerated charge carriers can be described as:[24]

$$SC + h\nu \rightarrow e^- + h^+ \quad (h\nu = \text{SC band gap}) \tag{2}$$

$$CH_3CH_2OH + 2* \rightarrow CH_3CH_2O^-_{(ads)} + H^+_{(ads)} \tag{3}$$

where * represents an available adsorption site on the SC surface. The reaction proceeds through the abstraction of a second hydrogen atom from the resulting alkoxide via reaction with a photoproduced hole:

$$CH_3CH_2O^-_{(ads)} + h^+ \rightarrow CH_3CHO_{(ads)} + H^+_{(ads)} + e^- \tag{4}$$

Finally, proton reduction leads to the formation of molecular hydrogen, that eventually desorbs from the SC surface:

$$2H^+_{(ads)} + 2e^- \rightarrow H_{2\,(ads)} \rightarrow H_{2(g)} \tag{5}$$

The weak interaction of acetaldehyde with the SC surface results in its fast desorption, and its high volatility precludes the occurrence of further photo-oxidation processes. This explains why, in the case of ethanol, no carbon dioxide was detected. In a different way, polyhydroxylated molecules, such as glycerol or glucose, can undergo multiple oxidation steps, making the process more complex and more sensitive to the presence of surface vacancies acting as adsorption sites (see below).

To attain a deeper insight into the β- and ε-Fe_2O_3 activity in H_2 generation, a detailed structural investigation was carried out by transmission electron microscopy (TEM). **Figure 2**a shows that both β- and ε-Fe_2O_3 are polycrystalline materials exhibiting a columnar-like growth. Cross-sectional (cs) and plane-view (pv) electron diffraction (ED) patterns could be indexed according to cubic *Ia-3* (206) β-Fe_2O_3 (PDF card 00–039–0238) and orthorhombic $Pna2_1$ (33) ε-Fe_2O_3 (ICSD card

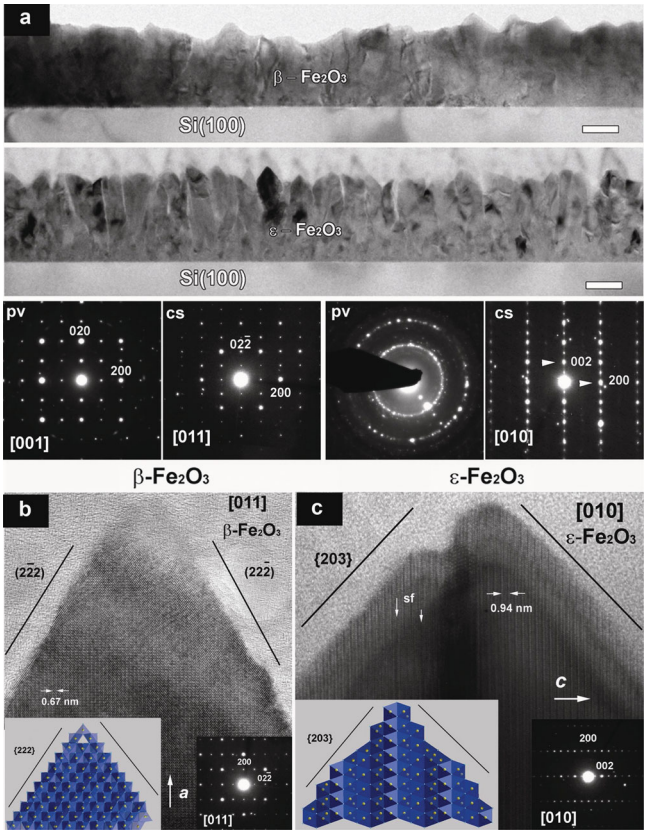

Figure 2. a) Cs bright-field TEM images of β- and ε-Fe_2O_3 (scale bars = 200 nm), with corresponding pv and cs ED patterns. b) HR-TEM image and ED pattern of a β-Fe_2O_3 aggregate, imaged along the [011] zone axis. c) HR-TEM image and ED pattern of a ε-Fe_2O_3 aggregate imaged along the [010] zone axis. Stacking faults are marked by white arrows. Insets: corresponding structural models (Fe = yellow spheres, O = light blue spheres).

51122). Figure 2b displays high resolution (HR)-TEM images and ED patterns of a representative β-Fe_2O_3 nanograin, imaged along the [011] zone axis, that showed a *V*-type shape and a predominant exposure of {222}-type surface planes. For ε-Fe_2O_3, the typical nanocrystal structure, imaged along the [010] zone axis, is shown in Figure 2c. In this case, the crystal *V*-type shape was related to the preferential exposure of {203}-like planes, and several stacking faults perpendicular to the *c*-axis could be observed. Structural models based on HR-TEM data and displaying the arrangement of FeO_6 octahedra are proposed in the insets of Figure 2b,c.

On the basis of the high β- and ε-Fe_2O_3 activity and stability in water/ethanol media, photocatalytic H_2 generation was also investigated starting from aqueous solutions of glycerol (**Figure 3**a) and glucose (Figure 3b), two relevant biomass-derived raw materials. In both cases, ε-Fe_2O_3 showed superior performances than β-Fe_2O_3. Furthermore, the obtained hydrogen yields were systematically lower in the case of glucose. A comparison of Figures 1 and 3 indicates that H_2 production rates decrease in the order ethanol > glycerol > glucose, that is, upon increasing the complexity of the organic molecule.[2,10]

As a matter of fact, the reactivity order of β- versus ε-Fe_2O_3 depends on both the used OOC and the photocatalyst nanoorganization, structure and defectivity.[3,5,15] The interpretation of the observed reactivity order is indeed a challenging issue, depending in a complex way on the interplay between catalytic reactivity, charge separation efficiency and different light harvesting by the used photocatalysts. In the present case, a thorough understanding of such phenomena is further complicated since the obtained Fe_2O_3 polymorphs are characterized by only moderate variations in chemico-physical properties. Hence, different complementary characterization tools have been used in the attempt to elucidate the observed reactivity differences between β- and ε-Fe_2O_3 phases on an atomic scale.

The main mechanism for the photo-oxidation of polyhydroxylated molecules (such as glycerol and glucose) over metal oxides involves direct electron transfer from the chemisorbed species to the photogenerated holes. The adsorption of polyhydroxylated OOCs on the photocatalyst surface is promoted by the molecule hydroxyl groups.[25,26] In this case, H_2 production from hydroxyl H atoms can proceed up to the complete degradation of the molecular skeleton involving progressive decarboxylation with CO_2 evolution, as well as the production

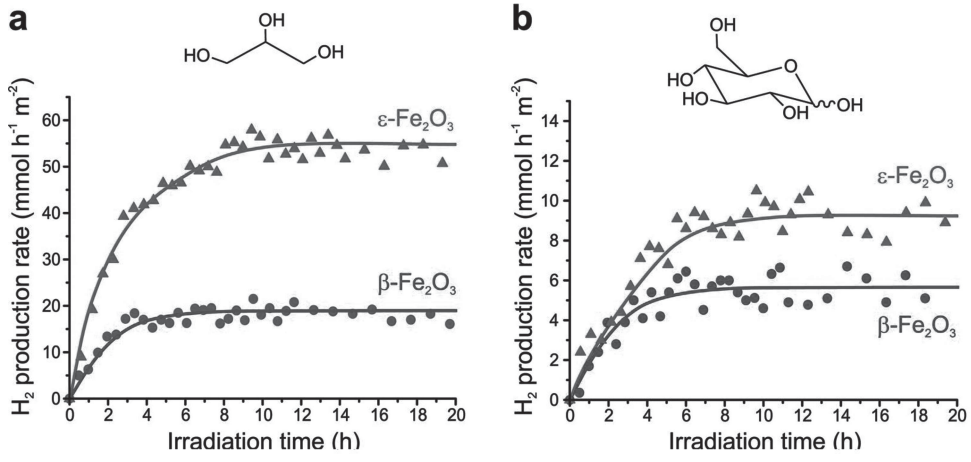

Figure 3. H_2 production rates from β- and ε-Fe_2O_3 by photoreforming of aqueous solutions containing a) glycerol and b) glucose, upon simulated sunlight irradiation.

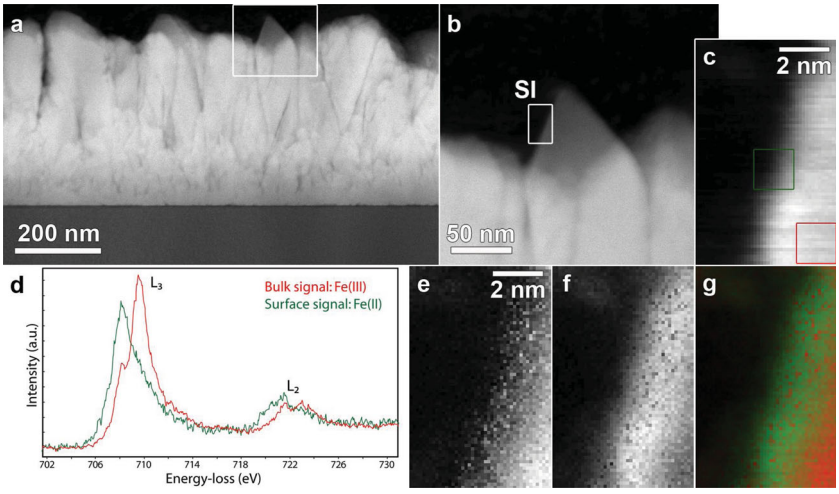

Figure 4. a) Overview HAADF-STEM image of ε-Fe_2O_3. b) Magnified HAADF-STEM image of the region indicated by the white box in (a). c) HAADF-STEM image collected simultaneously with EELS data on the single grain region indicated by the white rectangle in (b). d) Fe $L_{2,3}$ edge EELS spectra collected from the surface (green) and inner (red) regions of ε-Fe_2O_3. The red and green squares indicate the 12 × 12 pixel areas from which the data in (d) were averaged. e) Fe(III) and f) Fe(II) maps collected in the regions indicated by the white rectangle in (b). g) Colour map obtained by the superimposition of Fe(III) and Fe(II) maps shown in e) and f) (Fe(III) = red; Fe(II) = green).

of various intermediate compounds (Supporting Information, Figure S6 and Scheme S2).[2,8] In this context, the presence of oxygen vacancies can significantly affect the OOC chemisorption and subsequent decomposition, which influence, in turn, the resulting photocatalytic activity.[27]

In order to assess the possible presence of such defects on the target β- and ε-Fe_2O_3 nanomaterials, scanning TEM-electron energy loss spectroscopy (STEM-EELS) experiments were carried out using the spectrum imaging (SI) technique. This method consists in the simultaneous acquisition of an EELS spectrum and a high angle annular dark field (HAADF) signal by scanning different sample regions with a focused electron probe. The Fe $L_{2,3}$ EELS edge was investigated due to its high sensitivity towards iron local coordination environment and valence state.[28,29] **Figure 4**a presents an overview HAADF-STEM (*Z*-contrast) image of ε-Fe_2O_3. A typical single grain, displayed at higher magnification in Figure 4b, was selected for SI investigation (Figure 4c). Figure 4d shows the collected Fe $L_{2,3}$ EELS data. The spectrum corresponding to the inner region (bulk signal), with the L_3 maximum located at 709.5 eV and a pre-peak centred at 708.0 eV, is typical for Fe(III) in a predominantly (3 out of 4 Fe ions) octahedral environment, in line with ε-Fe_2O_3 crystal structure.[17,30] Repeated measurements on other aggregates always yielded the same results. Notably, the Fe $L_{2,3}$ edge fine structure underwent a significant change on going towards the surface (Figure 4d), with a peak shift to lower energy by 1.5 eV, indicating a partial Fe(III) → Fe(II) reduction in the outermost material layers.[30] This process was further supported by the concomitant decrease of L_3/L_2 intensity ratio. Since HR-TEM imaging did not evidence any crystal lattice variation near to the surface (compare Figure 2c), the observed valence change could be assigned to the extensive presence of oxygen vacancies at the ε-Fe_2O_3 surface.

In contrast to the case of ε-Fe_2O_3, EELS spectra collected on the surface and bulk regions of β-Fe_2O_3 indicated the lack of oxygen vacancies in appreciable amounts and the predominance of Fe(III) even in the outermost layers (Supporting Information, Figure S7). As a consequence, the outstanding activity of the β-phase in ethanol photoreforming (Figure 1) can be related to the stronger Lewis acidity of Fe(III) sites that, compared to Fe(II) centers, possess a higher ability to chemisorb and dehydrogenate ethanol.[31] In a different way, glycerol and glucose contain various –OH groups and hence can strongly bind to the oxide surface. Under these conditions, a high density of strongly acidic surface Fe(III) sites is not necessary to ensure an efficient adsorption, while the presence of oxygen vacancies favorably affects ε-Fe_2O_3 performances, promoting a more effective charge carrier separation and the subsequent accumulation of photogenerated electrons on the catalyst surface. Whereas these observations opens new research directions, a deep understanding of structure-property relationships is an open challenge that needs to be addressed in future studies.

In addition, compared to β-Fe_2O_3, the activity of the ε-phase also benefits from an enhanced light absorption due to its slightly lower band-gap. In fact, EELS measurements in the low energy-loss region allowed to estimate energy gap values of 2.4 and 2.2 eV for β- and ε-Fe_2O_3, respectively (Supporting Information, Figure S8a,b). In order to obtain a more detailed insight into the electronic structure of the three polymorphs and attain an estimation of their band edge positions with respect to water oxidation/reduction potentials, EELS data were combined with results obtained from XPS valence band (VB) analysis (Supplementary Figure S4b-d). Following a procedure similar to that of Chen et al.[21] and basing on EELS gap values, a relative energy level diagram could be constructed (Supporting Information, Figure S8c). The CB edges of the three polymorphs lie lower (more positive) than the redox potential of the H^+/H_2 couple (pH = 0), indicating that, under strongly acidic media, these materials are unsuitable for hydrogen generation, at least in the absence of an external bias. Nevertheless, since the present experiments were carried out in nearly neutral solutions (pH ≈ 7) and at room temperature, CB positions can be favorable for H^+ reduction to H_2, especially in the case of β-Fe_2O_3. Hence, electron–hole pairs photogenerated upon suitable irradiation can result in the effective oxidation of adsorbed OOCs (by VB holes) and in H^+ reduction (by CB electrons).

3. Conclusions

The data presented here demonstrate that β- and ε-Fe_2O_3 nanomaterials, two scarcely investigated iron oxide phases, possess a remarkable activity in sunlight-assisted H_2 generation by OOC photoreforming. Notably, up to now these two iron oxides

Table 1. Experimental conditions for the synthesis of various Fe_2O_3 polymorphs.

Polymorph	Total pressure (mbar)	O_2 flow [cm^3 min^{-1}]	Water vapor[a)]
α-Fe_2O_3	3.0	20	YES
β-Fe_2O_3	10.0	100	NO
ε-Fe_2O_3	10.0	100	YES

[a)]Water vapor is introduced using an auxiliary O_2 flow (same rates as in column 3) passing through a water reservoir maintained at 50 °C.

polymorphs have never been tested in H_2 generation experiments. The control of crystal phase and surface composition/defectivity has been proved to be a key issue for the fabrication of stable and efficient photocatalysts. The technological importance of the actual performances is strengthened by the use of supported nanomaterials, enabling to circumvent problems associated to powdered photocatalysts. The proposed approach holds a remarkable potential not only for a sustainable hydrogen production, but also for the simultaneous synthesis of added-value by-products, paving the way to manifold technological applications.

From a fundamental point of view, these results give clear evidence of the attractive performances of iron oxides as photocatalysts for hydrogen production. Interesting perspectives for advancements of the present activities will concern the identification of suitable preparation conditions for the selective fabrication of other iron(III) oxide polymorphs, such as γ-Fe_2O_3, or other iron oxides, such as Fe_3O_4, scarcely investigated for this application up to date. The extension of the present study to such systems is undoubtedly a key point to gain a thorough and rational understanding of structure-reactivity interrelations in the Fe-O system.

4. Experimental Section

Sample Preparation: A cold-wall horizontal CVD apparatus[32] was used for iron oxide deposition, starting from $Fe(hfa)_2TMEDA$ (hfa = 1,1,1,5,5,5-hexafluoro-2,4-pentanedionate, TMEDA = *N*,*N*,*N*′, *N*′ – tetramethylethylenediamine) as iron precursor.[16] The compound, placed in a vaporization vessel (0.3 g for each growth experiment), was heated by means of an oil bath and vaporized at 60 °C. Depositions were carried out on HF-etched *p*-type Si(100) substrates (MEMC, Merano, Italy, 10 mm × 10 mm × 1 mm). In view of an eventual process scale-up, the use of the cheaper Si(100) supports has been preferred over the more conventional F-doped tin oxide (FTO) or Indium Tin Oxide (ITO), usually adopted for photoelectrodes, since no electrical signal had to be applied (or recorded from) to the present photocatalysts.

The obtainment of the three Fe_2O_3 polymorphs was achieved under optimized conditions, as reported in **Table 1**. The deposition time and growth temperature were set at 60 min and 500 °C, respectively.

Characterization Techniques: Glancing incidence X-ray diffraction (GIXRD) analyses were performed by a Bruker D8 Advance diffractometer, using a Cu Kα source (λ = 1.5418 Å), at a fixed incidence angle of 1.0°.

Atomic force microscopy (AFM) images were obtained by a NT-MDT SPM Solver P47H-PRO instrument operating in tapping mode and in air. After a plane fitting procedure, root mean square (RMS) roughness values were estimated on 2 μm × 2 μm images.

Plane-view (pv) and cross-sectional (cs) FE-SEM images were collected by a Zeiss SUPRA 40VP field emission instrument, at primary beam voltages comprised between 10.0 and 20.0 kV. Line-scan EDXS analyses were carried out by monitoring the Fe Kα, O Kα, and C Kα signals throughout the deposit thickness by an Oxford INCA x-sight X-ray detector (acceleration voltage 20.0 kV).

XPS analyses were carried out by a Perkin-Elmer Φ5600ci spectrometer at pressures lower than 1×10^{-8} mbar, using a standard Al Kα source ($h\nu$ = 1486.6 eV). The reported BEs (standard deviation = ± 0.1 eV) were corrected for charging effects by assigning to the C1s line of adventitious carbon a position of 284.8 eV. Quantitation was performed using sensitivity factors provided by Φ V5.4A software.

Specimens for TEM observations were prepared by mechanically grinding down to 20 μm, followed by Ar^+ ion beam milling using a Balzers RES 101 GVN apparatus. TEM and HR-TEM analyses were performed using a Tecnai G2 30 UT microscope at 300.0 kV, with a 0.17 nm point resolution.

HAADF-STEM and STEM-EELS experiments were carried out on a Titan "cubed" microscope, equipped with an aberration corrector, a monochromator and a high-resolution GIF QUANTUM energy filter. For STEM-EELS analyses, the microscope was operated at 120 kV. The electron monochromator was excited to provide an estimated EELS energy resolution of 250 meV. The internal Fe(II) and Fe(III) references were back-fitted to the EELS data cube using the EELS model software [www.eelsmodel.ua.ac.be], to generate Fe(II) and Fe(III) maps. The convergence angle used in the STEM-EELS experiments was 21 mrad, while the acceptance angles for EELS analyses and HAADF imaging were 160 and 85 mrad, respectively.

Photocatalytic Activity Measurements: The photoreforming activity was evaluated under simulated sunlight irradiation (Supporting Information, Figure S9), using a solar simulator (LOT-Oriel) equipped with a 150 W Xe lamp and an atmospheric edge filter to cut-off UV photons below 300 nm. The beam was focused on the sample and the resulting light intensity was ≈25 mW cm^{-2} (250–400 nm, UV-A) and ≈180 mW cm^{-2} (400–1000 nm, Vis-NIR). The incident illumination power, though close to twice of a standard AM1.5, is representative of a simple but effective solar concentrator. Specimens were placed at the bottom of the reactor (maintained at 25 °C) filled with 80 mL of a water/OOC solution. The OOC concentrations (ethanol 8.5 M, glycerol 1.0 M, and glucose 5.5×10^{-2} M) were chosen in order to simulate aqueous solutions recovered from biomass treatments. Evolved gaseous products were stripped by an Ar flow (15 mL min^{-1}) and detected on-line by an Agilent 7890 gas chromatographer. A Carboxen 1010 PLOT column (Supelco, 30 m × 0.53 mm ID, 30 μm film) connected to a thermal conductivity detector (TCD) was used for H_2 analysis, using Ar as carrier gas. Basing on the sample geometrical area, H_2 production rates were expressed as mmol h^{-1} m^{-2} (uncertainty: ± 0.3 mmol h^{-1} m^{-2}). Hydrogen yields normalized for the catalyst amount were calculated basing on thickness values (see also the main text), considering the specimens as compact and continuous deposits and assuming Fe_2O_3 bulk densities (5.3, 5.1, and 4.8 g cm^{-3} for α-, β-, and ε-Fe_2O_3, respectively).

The analysis of volatile compounds in the gas flow (carrier gas: He) was performed using a DB522-ms capillary column (J&W, 60 m × 0.32 mm ID, 20 μm film) connected to an Agilent 5975C mass spectrometry (MS) detector.

Liquid fractions after photoreforming experiments were analyzed using the same instrument (Agilent 7890 with 5975C MS detector and DB522-ms column).

SFE values were calculated using the formula adapted from Reece et al.:[33]

$$SFE = \frac{\Delta E}{S} \times 100 \quad (6)$$

where ΔE is the energy stored in the amount of H_2 produced by photoreforming and S is the total incident solar irradiance, as measured by adequate radiometers in the UV and Vis spectral ranges (expressed in W cm^{-2}). ΔE is calculated as the amount of H_2 produced by each sample

(expressed in mol s^{-1} cm^{-2}) multiplied by hydrogen combustion enthalpy (285.8 kJ mol^{-1} at 298 K).

Graphite-furnace atomic absorption spectroscopy (GF-AAS) was used to quantify the iron amount leached during photocatalytic experiments. After filtration using 0.22 µm PVDF membranes, 5 µL of the solutions were diluted with 15 µL of MilliQ water and injected into the furnace.

Supporting Information

Supporting Information is available from the Wiley Online Library or from the author.

Acknowledgements

G.C., C.M., A.G., and D.B. acknowledge financial support from the European Community's Seventh Framework Program (FP7/2007–2013, ENHANCE-238409), as well as from Regione Lombardia-INSTM ATLANTE, University of Padova ex-60% 2012 (60A03–5517), PRAT 2010 (CPDA102579) and Fondazione Cariparo (Nano-Mode, 2010) projects. T.M., V.G., G.A., and P.F. acknowledge financial support from the University of Trieste through FRA 2011 project, as well as from INSTM, ICCOM-CNR Progetti Premiali, Fondazione CRTrieste, Fondazione Benefica Kathleen Foreman Casali and COST Action 1104. S.T., O.I.L., and G.V.T. acknowledge financial support from the European Research Council under the Seventh Framework Program (FP7), ERC grant N° 246791 – COUNTATOMS. S.T. and G.V.T. acknowledge financial support from the Fund for Scientific Research Flanders (FWO, project N° G004613N) and Hercules Foundation. A unit on page 377 was corrected on January 22, 2014.

Received: June 14, 2013
Revised: July 30, 2013
Published online: September 16, 2013

[1] G. Ciamician, *Science* **1912**, *36*, 385.
[2] M. Cargnello, A. Gasparotto, V. Gombac, T. Montini, D. Barreca, P. Fornasiero, *Eur. J. Inorg. Chem.* **2011**, *2011*, 4309.
[3] B. D. Alexander, P. J. Kulesza, I. Rutkowska, R. Solarska, J. Augustynski, *J. Mater. Chem.* **2008**, *18*, 2298.
[4] X. Chen, S. Shen, L. Guo, S. S. Mao, *Chem. Rev.* **2010**, *110*, 6503.
[5] R. M. N. Yerga, M. C. A. Galván, F. del Valle, J. A. V. de la Mano, J. L. G. Fierro, *ChemSusChem* **2009**, *2*, 471.
[6] A. Kudo, Y. Miseki, *Chem. Soc. Rev.* **2009**, *38*, 253.
[7] K. Jun, Y. S. Lee, T. Buonassisi, J. M. Jacobson, *Angew. Chem. Int. Ed.* **2012**, *51*, 423.
[8] D. I. Kondarides, V. M. Daskalaki, A. Patsoura, X. E. Verykios, *Catal. Lett.* **2008**, *122*, 26.
[9] M. Bowker, *Catal. Lett.* **2012**, *142*, 923.
[10] X. Fu, J. Long, X. Wang, D. Y. C. Leung, Z. Ding, L. Wu, Z. Zhang, Z. Li, X. Fu, *Int. J. Hydrogen Energy* **2008**, *33*, 6484.
[11] Q. Gu, X. Fu, X. Wang, S. Chen, D. Y. C. Leung, X. Xie, *Appl. Catal. B-Environ.* **2011**, *106*, 689.
[12] A. Patsoura, D. I. Kondarides, X. E. Verykios, *Catal. Today* **2007**, *124*, 94.
[13] N. Strataki, V. Bekiari, D. I. Kondarides, P. Lianos, *Appl. Catal. B-Environ.* **2007**, *77*, 184.
[14] M. J. Katz, S. C. Riha, N. Cheon Jeong, A. B. Martinson, O. K. Farha, J. T. Hupp, *Coord. Chem. Rev.* **2012**, *256*, 2521.
[15] K. Sivula, F. Le Formal, M. Grätzel, *ChemSusChem* **2011**, *4*, 432.
[16] D. Barreca, G. Carraro, A. Devi, E. Fois, A. Gasparotto, R. Seraglia, C. Maccato, C. Sada, G. Tabacchi, E. Tondello, A. Venzo, M. Winter, *Dalton Trans.* **2012**, *41*, 149.
[17] L. Machala, J. Tucek, R. Zboril, *Chem. Mater.* **2011**, *23*, 3255.
[18] G. Carraro, D. Barreca, E. Comini, A. Gasparotto, C. Maccato, C. Sada, G. Sberveglieri, *CrystEngComm* **2012**, *14*, 6469.
[19] H. Bahruji, M. Bowker, P. R. Davies, L. S. Al-Mazroai, A. Dickinson, J. Greaves, D. James, L. Millard, F. Pedrono, *J. Photochem. Photobiol. A* **2010**, *216*, 115.
[20] M. de Oliveira Melo, L. Almeida Silva, *J. Photochem. Photobiol. A* **2011**, *226*, 36.
[21] X. Chen, L. Liu, P. Y. Yu, S. S. Mao, *Science* **2011**, *331*, 746.
[22] A. Gallo, T. Montini, M. Marelli, A. Minguzzi, V. Gombac, R. Psaro, P. Fornasiero, V. Dal Santo, *ChemSusChem* **2012**, *5*, 1800.
[23] R. Prucek, M. Hermanek, R. Zboril, *Appl. Catal. A* **2009**, *366*, 325.
[24] P. Pichat, M.-N. Mozzanega, H. Courbon, *J. Chem. Soc., Faraday Trans. I* **1987**, *83*, 697.
[25] I. A. Shkrob, T. W. Marin, S. D. Chemerisov, M. D. Sevilla, *J. Phys. Chem. C* **2011**, *115*, 4642.
[26] X. Fu, X. Wang, D. Y. C. Leung, Q. Gu, S. Chen, H. Huang, *Appl. Catal. B-Environ.* **2011**, *106*, 681.
[27] T. L. Thompson, J. T. Yates, *Top. Catal.* **2005**, *35*, 197.
[28] R. F. Egerton, *Electron energy-loss spectroscopy in the electron microscope*, 3rd ed., Springer, New York, **2011**.
[29] H. Tan, J. Verbeeck, A. Abakumov, G. Van Tendeloo, *Ultramicroscopy* **2012**, *116*, 24.
[30] P. A. Van Aken, B. Liebscher, *Phys. Chem. Miner.* **2002**, *29*, 188.
[31] A. Glisenti, G. Favero, G. Granozzi, *J. Chem. Soc., Faraday Trans.* **1998**, *94*, 173.
[32] D. Barreca, A. Gasparotto, C. Maragno, E. Tondello, C. Sada, *Chem. Vap. Deposition* **2004**, *10*, 229.
[33] S. Y. Reece, J. A. Hamel, K. Sung, T. D. Jarvi, A. J. Esswein, J. J. H. Pijpers, D. G. Nocera, *Science* **2011**, *334*, 645.